Complex magnetic transitions in the triangular net compound $GdAl_2Ge_2$

Keke Feng [1], Melissa G. Anderson [2], Marcin Rosmus [3], Alexandre Antezak [3], Christopher Farago [4], Emmanouil Frantzeskakis [3], Franck Fortuna [3], Andres F. Santander-Syro [3], Gregory T. McCandless,[2] Julia Y. Chan [2], and Ryan E. Baumbach [4]

[1]*Department of Physics, UC San Diego, San Diego, California 92093, USA*
[2]*Department of Chemistry and Biochemistry, Baylor University, Waco, Texas 76798, USA*
[3]*Université Paris-Saclay, CNRS, Institut des Sciences Moléculaires d'Orsay, 91405 Orsay, France*
[4]*Department of Physics, UC Santa Cruz, Santa Cruz, California 95060, USA*

(Received 16 December 2025; revised 23 February 2026; accepted 3 March 2026; published 21 April 2026)

Thermodynamic and electrical transport properties are reported for single crystals of the trigonal $GdAl_2Ge_2$, where complex antiferromagnetic ordering is seen at $T_{N1} = 23.3$ K and $T_{N2} = 20.8$ K and a rich phase diagram is revealed under applied magnetic fields. Angle-resolved photoemission spectroscopy (ARPES) measurements provide insights into this behavior by revealing a threefold symmetric Fermi surface that reflects the trigonal space-group symmetry. This promotes competing long-range Ruderman-Kittel-Kasuya-Yosida (RKKY) interactions between localized magnetic moments and is associated with the appearance of fine tuned ordered states. This is accompanied by intrinsic null orbital angular momentum ($L = 0$ for trivalent Gd), which yields Heisenberg spins and ensures that the symmetry of the Fermi surface dominates the magnetic behavior over wide temperature ranges. Comparisons are made to related triangular-net f-electron materials, providing guidance for understanding their diverse behaviors.

DOI: 10.1103/kjct-68sj

I. INTRODUCTION

Systems that combine novel electronic band structures with correlated lattice, charge, and spin degrees of freedom continue to attract interest as reservoirs for functional electronic and magnetic phenomena, including the anomalous/topological Hall effect [1–3], unconventional superconductivity [4–6], skyrmion lattice formation [3,7,8], altermagnetism [9–11], and more. Triangular-net lattices are paradigmatic examples, where the lattice geometry is associated with tunable competitions between the magnetic, electronic, orbital, and bonding degrees of freedom. Example systems include the semimetallic Zintl compound $EuCd_2As_2$, which may be a magnetic Weyl semimetal [12,13]; Gd_2PdSi_3, which hosts skyrmions at low temperatures [3,14,15]; and delafossite-variant compounds $ALnX_2$ (A = alkali metal, Ln = lanthanide, and X = chalcogenide), which are being pursued as hosts for geometric and bond frustration [16–18].

Here, we report results for $GdAl_2Ge_2$, which crystallizes in the trigonal $CaAl_2Si_2$ structural prototype (space group $P\bar{3}m1$) and features planar triangular nets of Gd ions (Fig. 1) [19]. Magnetization, heat capacity, and electrical resistivity measurements reveal metallic behavior and typical Curie-Weiss paramagnetism at elevated temperatures, where fits to the data yield a negligible Curie-Weiss temperature ($\theta \approx -1$ K). For a conventional mean-field paramagnet, this would indicate a weak antiferromagnetic exchange interaction between the Gd ions that would be expected to produce ordering at a commensurately low temperature. Instead, here we find evidence for strong spin fluctuations that are followed by complex antiferromagnetic-like ordering at the transition temperatures, $T_{N1} = 23.3$ K and $T_{N2} = 20.8$ K. This shows that strong magnetic interactions are present, and that competition between them likely produces the small θ value. Heat capacity measurements indicate that the two transitions are second order and first order, respectively. Applied magnetic fields produce rich phase diagrams, where T_{N1} is suppressed in a manner that is consistent with antiferromagnetic-like order, but evidence for competing interactions is seen in (i) the anisotropic evolution of T_{N2} vs H and (ii) the appearance of several hysteretic spin reorientation transitions at low magnetic fields. These results provide evidence both for non-mean-field magnetism (evidenced by $\theta/T_N << 1$) and magnetically ordered states that are potentially characterized by nontrivial order parameters.

Angle-resolved photoemission spectroscopy (ARPES) measurements provide further insights by uncovering a Fermi surface that consists of a small hole-like pocket that is centered at the $\bar{\Gamma}$ point and large threefold symmetric electron-like pockets located around $\bar{M}$ and $\bar{M}'$. Corresponding features are seen for the structural relatives $LnAuAl_4Ge_2$ [20,21], pointing towards a shared Ruderman-Kittel-Kasuya-Yosida (RKKY) interaction [22–24] mediated by the conduction electrons, and hence governed by the Fermi surface geometry. This leads to enhanced spin fluctuations, multiple transitions, and complex T–H phase diagrams throughout this entire family [21,25,26]. In most cases, spin-orbit coupling and crystal electric field effects also play symmetry-breaking roles that impact the ordering. However, for the Gd-based examples, the null value of the orbital angular momentum ($L = 0$) ensures that the Fermi surface symmetry alone dominates the paramagnetism and eventual formation of the ordered states. Based on this, we propose that $GdAl_2Ge_2$ provides a minimally constrained environment for RKKY driven competition,

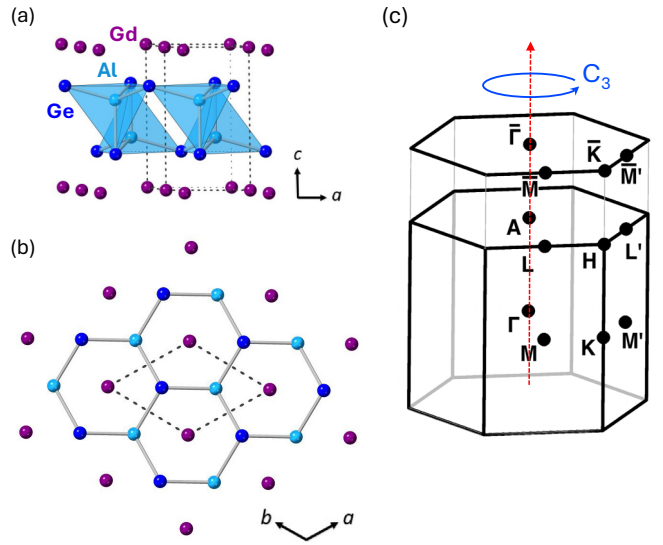

FIG. 1. Summary of crystal structure and symmetry for $GdAl_2Ge_2$. (a), (b) Side and top view of the $GdAl_2Ge_2$ crystal structure, where the purple spheres represent Gd atoms, light blue spheres represent Al atoms, and dark blue spheres represent Ge atoms. (c) Brillouin zone of $GdAl_2Ge_2$ and its surface projection. Despite the apparent hexagonal symmetry of the Brillouin zone, the out-of-plane (kz) axis is an axis of threefold symmetry for the electronic structure, following the symmetry of the space group.

whose symmetry mimics the trigonal symmetry of the lattice, thereby leading to the mean-field breakdown and the eventual emergence of multiple magnetic order parameters.

II. EXPERIMENTAL METHODS

$GdAl_2Ge_2$ single crystals were grown using the molten metal flux method following the procedure detailed in Ref. [25]. Copper was included in the melt in an attempt to produce $GdCuAl_4Ge_2$, but $GdAl_2Ge_2$ emerged instead. Crystals form as three-dimensional clusters, where individual pieces with dimensions on the order of 2 mm and either hexagonal or triangular facets associated with the *ab* plane can be isolated. For single-crystal x-ray diffraction measurements, a small ($0.01 \times 0.01 \times 0.02$ mm^3) fragment was mounted on a glass fiber. Data were collected at room temperature using a Bruker D8 Quest Kappa X-ray Diffractometer equipped with a IμS microfocus source (Mo Kα, $\lambda = 0.71073$ Å), HELIOS optics monochromator, and a PHOTON III CPAD detector. Integration of the data was performed using the Bruker SAINT program and a multiscan method from the SADABS 2016/2 program was used for intensity absorption correction [27]. A preliminary starting model was generated using SHELXT [28] and then SHELXL [29] was used to refine the model anisotropically with the refinement parameters listed in Table 1 in the Supplemental Material (SM) [30] (see also [31] references therein), resulting in the atomic positions in Table 2, also in the SM [30].

These measurements confirm that $GdAl_2Ge_2$ crystallizes in the trigonal $CaAl_2Si_2$-type structure (Fig. 1) [19]. As previously reported, $GdAl_2Ge_2$ contains an Al_2Ge_2 polyanion, described as aluminum atoms tetrahedrally coordinated by germanium atoms. The polyanionic framework is surrounded by gadolinium atoms on the corners of the unit cell. Additionally, the Al_2Ge_2 polyanion may be visualized as hexagonal layers of alternating aluminum and germanium atoms in the c direction [Fig. 1(b)]. The Gd–Ge interatomic distances are shorter than Gd-Al interatomic distances (Table 3 within the SM [30]) because of the puckering of these slightly distorted Al/Ge hexagons. Reflections present in the precession images are indexed based on a unit cell determined for our single-crystal x-ray diffraction model. Energy-dispersive spectroscopy (EDS) was performed using a VERSA 3D focused ion beam scanning electron microscope with a voltage of 30 keV. The average (normalized to Gd) of five scans on select points of the crystal yields the formula $Gd_{1.0(1)}Al_{2.4(5)}Ge_{1.8(3)}$ in agreement with the single-crystal x-ray diffraction model.

Temperature-dependent magnetic susceptibility measurements $\chi(T) = M/H$ were carried out for $T = 1.8$–300 K under magnetic fields $H = 0.05$–5 T applied parallel ($\parallel$) and perpendicular ($\perp$) to the crystallographic c axis using a Quantum Design VSM Magnetic Property Measurement System. Data were collected (i) under zero-field-cooled (ZFC) conditions, where the sample was cooled to $T = 1.8$ K, the magnetic field was applied, and M was measured as T increased to 300 K and (ii) field-cooled (FC) conditions, where the magnetic field was applied at 300 K and M was measured as T decreased to 1.8 K. Heat capacity C measurements were performed for $T = 1.8$–200 K in a Quantum Design Physical Properties Measurement System using a conventional thermal-relaxation technique. Electrical resistivity ρ measurements for $T = 1.8$–300 K and magnetic fields $\mu_0 H \leqslant 9$ T were performed in a four-wire configuration for a polished single crystal using the same system. For $\rho(T)$, both ZFC and FC conditions were measured. For $\rho(H)$, samples were zero-field-cooled prior to measurements.

Angle-resolved photoemission spectroscopy (ARPES) studies were performed at the Cassiopée beamline (SOLEIL synchrotron, France), which is equipped with a Scienta R4000 photoelectron energy analyzer. The samples were cleaved in situ under ultrahigh vacuum at 16 K. During the ARPES measurements, the pressure remained below 3×10^{-10} mbar, and unless stated otherwise, the temperature was maintained at 16 K.

III. RESULTS

Figure 2 summarizes the temperature and magnetic field dependent magnetization of $GdAl_2Ge_2$. Curie-Weiss behavior is observed at elevated temperatures, where the data are described by the expression $\chi(T) = C/(T - \theta)$. Fits to the data for 25 K $< T <$ 300 K reveal that the effective magnetic moment $\mu_{\text{eff}} = 2.82\sqrt{C} = 7.8\,\mu_B$/Gd for $H \parallel$ and $\perp$ c, which is close to the expected value for Gd^{3+} ($\mu_{\text{eff}} = 8.0$ μ_B/Gd^{3+}). The fits also yield $\theta_\parallel \approx \theta_\perp = -1 \pm 0.1$ K, which for a conventional mean-field system would suggest weak antiferromagnetic spin-exchange interactions and little anisotropy in the paramagnetic state. Despite this, complex magnetic ordering appears at temperatures well above θ [Figs. 2(d) and 2(e)], showing that θ does not reflect the true exchange-interaction strength. For $H \parallel c$, the ordering is seen as a knee

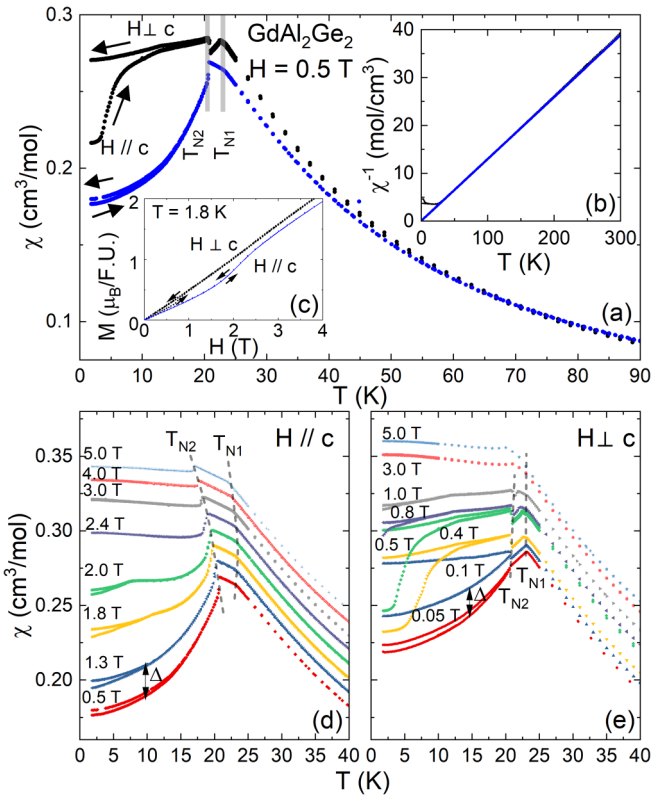

FIG. 2. Temperature and magnetic-field-dependent properties of $GdAl_2Ge_2$. (a) Magnetic susceptibility of $GdAl_2Ge_2$ with the field H = 0.5 T applied pendicular $\perp$ and parallel $\parallel$ to the c axis. (b) Inverse magnetic susceptibility $\chi^{-1}(T)$ vs T. The solid line is a fit to the data as described in the text. (c) Magnetization vs field $M(H)$ at T = 1.8 K for $H \parallel$ and $\perp c$. (d) $\chi(T)$ for $H \parallel$ c for magnetic fields H = 0.05–5 T. (e) $\chi(T)$ for $H \perp$ c for magnetic fields H = 0.05–5 T. Data at different H are shifted vertically for clarity. Ordering temperatures at T_{N1} and T_{N2} are labeled, where dotted lines provide guides to the eye.

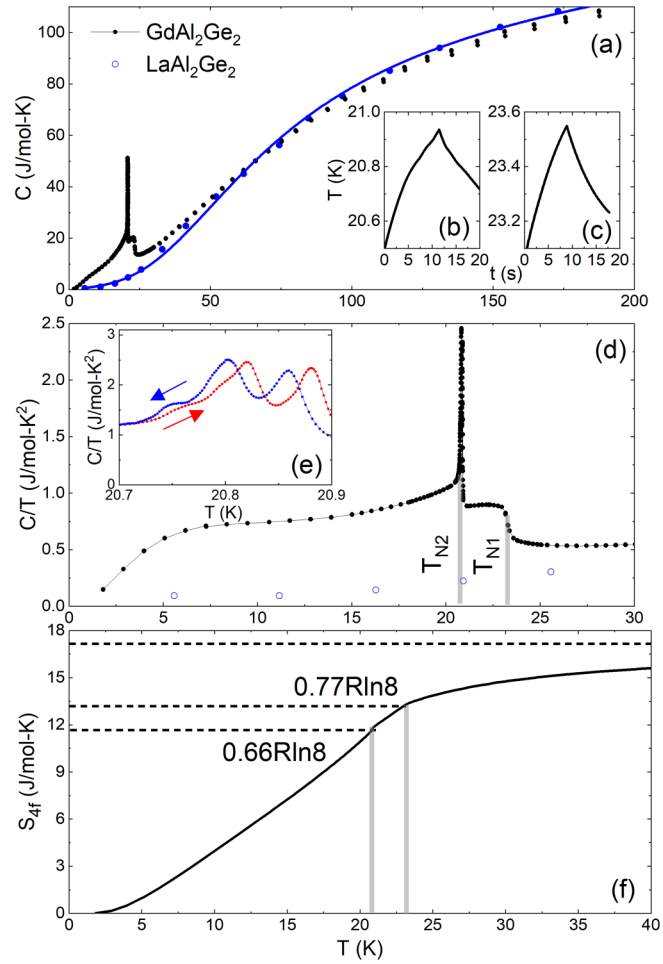

FIG. 3. Temperature-dependent heat capacity and entropy for $GdAl_2Ge_2$. (a) The heat capacity C vs T for $GdAl_2Ge_2$ at T = 1.8–200 K. Data are compared to results for the nonmagnetic analog $LaAl_2Ge_2$ (from Ref. [32]). (b), (c) Temperature vs time $T(t)$ relaxation curves in the vicinity of T_{N1} and T_{N2}. (d) C/T near the ordering temperatures T_{N1} and T_{N2}, where data were reanalyzed as described in the text the account for the latent heat of the transition at T_{N1}. (e) Zoom of C/T showing hysteresis near T_{N2}. The red and blue curves are for temperature rising and falling, respectively. (f) Magnetic entropy S_{mag} vs T for $GdAl_2Ge_2$.

at T_{N1} = 23.3 K and a step-like decrease at T_{N2} = 20.8 K that is followed by hysteresis at lower temperatures for $H \lesssim$ 2.4 T. For $H \perp c$, the ordering in small fields is seen as a decrease at T_{N1} = 23.3 K that is followed by another decrease at T_{N2} = 20.8 K; but for 0.1 $\lesssim H \lesssim$ 1 T, the feature at T_{N2} becomes a hysteretic step-like increase. This both reveals the presence of magnetic exchange interactions at an energy scale well above $k_B\theta$ and suggests that the ordered spin structures have an antiferromagnetic-like character, but are nontrivial. Field-dependent magnetization measurements are shown in Fig. 2(c), where spin reorientation is seen at modest fields. Further measurements, such as neutron or x-ray scattering, are needed to fully quantify the order parameters and their variation with H.

The heat capacity C for $GdAl_2Ge_2$ and its nonmagnetic analog $LaAl_2Ge_2$ [32] are shown in Fig. 3(a), where there is qualitative agreement between them at elevated temperatures, as expected when phonons are the dominant term. Previously, a fit to the data for $LaAl_2Ge_2$ using the expression $C = \gamma T + C_{Debye}$ [where γT is the electronic contribution and C_{Debye} is the integral Debye function; blue solid line Fig. 3(a)] yielded $\gamma \approx 100$ mJ/mol-K^2 and the Debye temperature $\theta_D \approx 300$ K. Similar values are obtained for $GdAl_2Ge_2$ if the fit range is limited such that its lower bound is above the temperature range where magnetic fluctuations potentially influence the heat capacity ($T > 50$ K). Below this temperature, C/T for $GdAl_2Ge_2$ gradually separates from the $LaAl_2Ge_2$ curve, providing evidence for spin fluctuations. The data eventually exhibit a pair of abrupt features at T_{N1} and T_{N2}, consistent with these being distinct bulk phase transitions.

An examination of the heat-pulse relaxation curves $T(t)$ near T_{N1} indicates a second-order phase transition [insets in Figs. 3(b) and 3(c)], while the additional structure in $T(t)$ near T_{N2} reveals evidence for a latent heat, as expected for a first-order phase transition [33] To account for this, in the vicinity of T_{N1}, the data were analyzed using a single-slope expression, resulting in the curves shown in Fig. 3(d). A close examination of the temperature rising and falling curves additionally

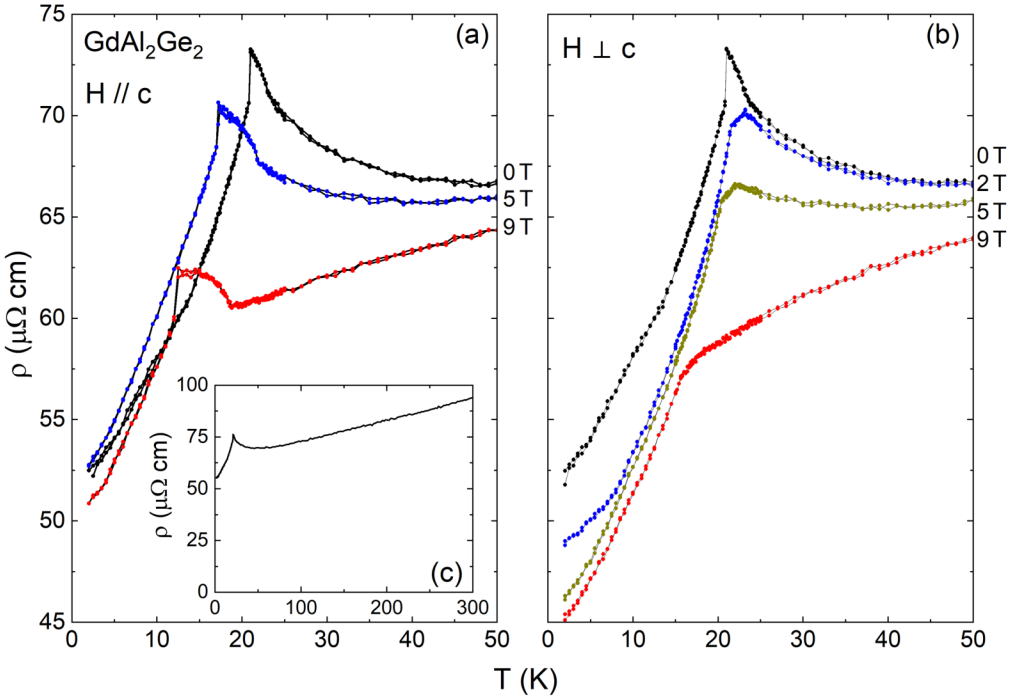

FIG. 4. Anisotropic temperature-dependent electrical transport for $GdAl_2Ge_2$. (a), (b) Temperature-dependent electrical resistivity $\rho(T)$ near the phase transitions at T_{N1} and T_{N2} for magnetic fields applied along the c axis ($H \parallel c$) and in the ab plane ($H \perp c$). (c) $\rho(T)$ for $T =$ 2–300 K and $H = 0$.

reveals hysteresis [Fig. 3(e)], as expected for first-order behavior. Finally, for $T < T_{N2}$, C/T exhibits a broad hump before falling towards small values as T approaches zero. This latter behavior is typical for Gd intermetallics where there are spin modes within the ordered state. To analyze the magnetic entropy, the $LaAl_2Ge_2$ curve was subtracted from the $GdAl_2Ge_2$ curve [$C_{mag}/T = C_{Gd}/T - (\gamma T + C_D/T)$] and the result was integrated [$S_{mag}(T) = \int_0^T C_{mag}/T\, dT$] [Fig. 3(f)]. This reveals that 66% and 77% of $R\ln 8$ are recovered at T_{N2} and T_{N1}, respectively. Finally, $S_{mag}(T)$ gradually increases above the ordered state and approaches the $R\ln 8$ value that is expected for $J = 7/2$ Gd^{3+}. This behavior may be attributed to additional S_{mag} at low temperatures or the continuation of magnetic fluctuations to temperatures above the ordered state.

The temperature-dependent electrical resistivity $\rho(T)$, measured for magnetic fields applied both along the c axis and in the ab plane, is summarized in Fig. 4. For $H = 0$, the room-temperature resistivity is near 90 μΩ cm and gradually decreases with decreasing T. A weak minimum develops near 50 K, consistent with trends in the heat capacity that indicate the presence of spin fluctuations for $T > T_{N1}$. Following this, the transitions at T_{N1} and T_{N2} produce an increase and a decrease in ρ, respectively, consistent with commensurate changes in the scattering of conduction electrons within the ab plane. Finally, ρ gradually decreases and saturates towards a residual resistivity near 50 μΩ cm. The large value of ρ_0 would typically be associated with intrinsic disorder scattering, but both x-ray diffraction and angle-resolved photoemission spectroscopy measurements indicate low disorder. This points towards the presence of spin-disorder scattering even below the ordering temperatures. Anisotropic electrical responses to the magnetic field are observed. For $H \parallel c$: T_{N1} and T_{N2} retain their characteristic shapes while being suppressed towards lower temperatures as H increases. For $H \perp c$: T_{N1} and T_{N2} are suppressed with increasing H, but the feature at T_{N1} rapidly evolves into a reduction in ρ while the feature at T_{N2} broadens into a smooth shoulder. These trends suggest that the spin order parameters feature additional direction-dependent competition, as indicated by the $\chi(T)$ measurements.

To clarify this behavior, Fig. 5 shows the magnetoresistance $\rho(H)$ for $H \parallel$ and $\perp$ to the c axis. Curves are shown both for field-rising and field-falling measurements. At the lowest temperatures, $\rho(H)$ for $H \parallel c$ initially has a weak field dependence and undergoes a rapid increase near H_1. This is followed by a decrease towards a kink at a second feature that we label H_2, after which $\rho(H)$ gradually decreases with negative curvature. The falling-field data trace these features down to H_1, where they separate from the field-rising curve and instead saturates towards a constant value with decreasing H. This pattern persists with increasing T, with H_1 and H_2 being gradually suppressed and merging near 13 K. An additional sharp increase appears at high field for 13 K $> T$ that we label H_3. Related behavior is seen for $H \perp c$, where hysteresis is again seen for $H < H_1$, followed by a decrease near H_2. While the feature at H_1 persists to T_{N2}, H_2 is suppressed with increasing T and collapses near 13 K. For $T > 16$ K, a kink at H_3 again becomes visible.

Figure 6(a) presents the experimental Fermi surface (FS) of $GdAl_2Ge_2$ measured at a photon energy of $h\nu = 45$ eV. The high-quality ARPES results attest to the highly crystalline structure of the single crystals. The Fermi surface

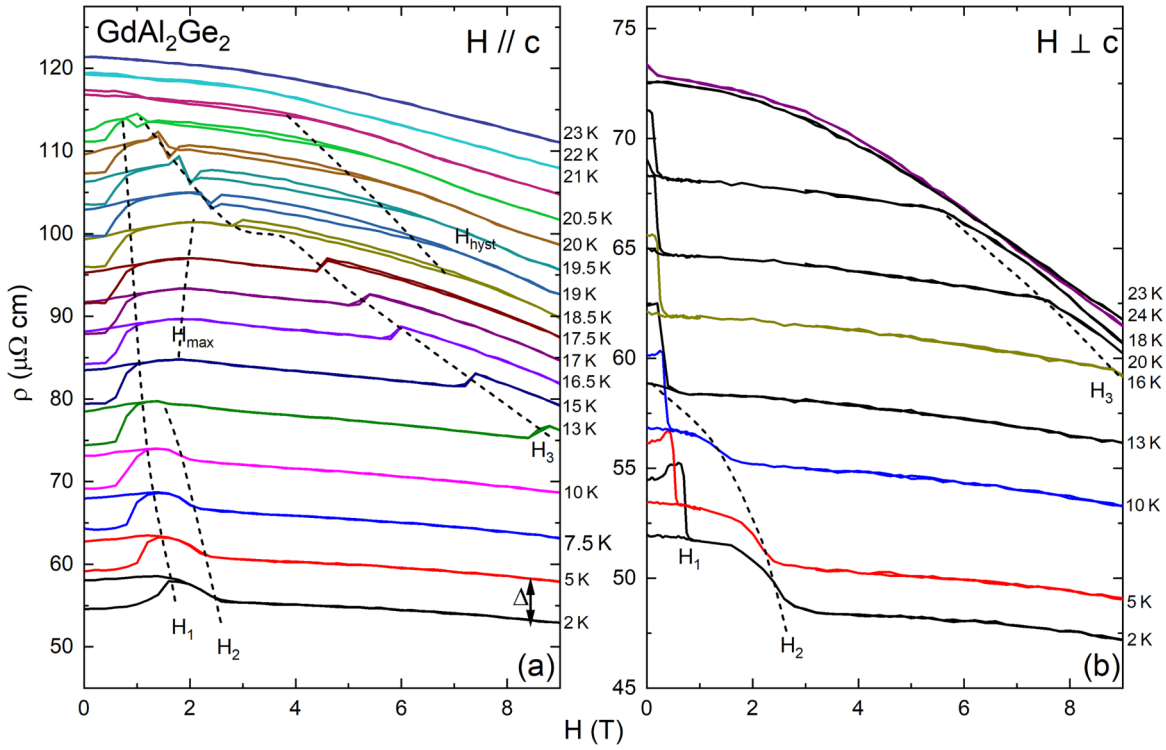

FIG. 5. Anisotropic isothermal magnetoresistance for $GdAl_2Ge_2$. Isothermal magnetoresistance $\rho(H)$ at different temperatures for magnetic field applied (a) along the c axis ($H \parallel c$) and (b) perpendicular to the c axis ($H \perp c$). The electrical current remains in the ab plane for both cases.

data were obtained by summing measurements acquired with linear vertical (LV) and linear horizontal (LH) light polarizations, in order to minimize intensity variations due to extrinsic factors related to the matrix elements of the photoemission process [34]. The surface-projected Brillouin zone of $GdAl_2Ge_2$ is hexagonal (see Fig. 1) but the electronic structure has only threefold rotational symmetry reflecting the trigonal symmetry of the crystal structure's point group (D_{3d}). As a result, the $\bar{\Gamma}$-$\bar{M}$ and $\bar{\Gamma}$-$\bar{M}'$ directions are not equivalent, although they still indicate mirror planes. Further details on the experimentally-resolved electronic structure, and its symmetry, will be discussed in the next paragraphs.

The Fermi surface consists of a hole-like pocket centered at the $\bar{\Gamma}$ point and electron-like pockets located around $\bar{M}$ and $\bar{M}'$. The corresponding band structure along the $\bar{K}$-$\bar{\Gamma}$-$\bar{M}$-$\bar{K}$-$\bar{M}'$-$\bar{\Gamma}$ path is shown in Fig. 6(b). The hole pocket at $\bar{\Gamma}$ is formed by different bands that lie very close in energy. The symmetry of the electronic structure is most clearly reflected at the borders of the surface-projected Brillouin zone. There is strong spectral weight at $\bar{M}'$ at an approximate energy of –1.5 eV, which is absent at $\bar{M}$, but, most interestingly, there are notable differences at the Fermi level. More specifically, the bands that form the electron-like pockets around the $\bar{M}$ and $\bar{M}'$ points have very different energy minima (550 meV for $\bar{M}$, and 750 meV for $\bar{M}'$). Additionally, the pocket around the $\bar{M}$ point is formed by two bands, with the second band becoming apparent along the $\bar{M}$-$\bar{K}$ direction. These clear experimental differences at the $\bar{M}$ and $\bar{M}'$ points of the Brillouin zone demonstrate the threefold symmetry of the Fermi surface, which mediates and governs the balance of the magnetic RKKY interactions.

In order to search for explicit changes in the electronic structure of $GdAl_2Ge_2$ across the double phase transition, ARPES measurements were performed at two temperatures: 16 K and 30 K. Figures 6(c) and 6(d) compare the band structures at these temperatures, focusing on the bands crossing the Fermi level around $\bar{\Gamma}$ (c) and $\bar{M}$ (d). Energy distribution curves were extracted at the position of the Fermi momenta and they are compared in the rightmost panels of Figs. 6(c) and 6(d). Within our experimental energy resolution, no significant differences were observed between the measurements conducted below and above the phase transition. The absence of significant differences in the electronic structure across the magnetic transitions is in line with the experimental findings in $GdAuAl_4Ge_2$ [20], a compound that belongs to the same homologous series and shares the same building block with $GdAl_2Ge_2$: i.e., both compounds share (i) an identical triangular net arrangement of the f-elements (i.e., Gd) and (ii) a Fermi surface with triangular features, although only $GdAl_2Al_2$ has threefold symmetry.

IV. DISCUSSION

The magnetic susceptibility, heat capacity, and electrical transport measurements are used to construct the T–H phase diagrams shown in Fig. 7, where several distinct regions are observed (labeled I, II, and III). Region I is bounded by $T_{N2} \leqslant T \leqslant T_{N1}$, where T_{N1} is gradually suppressed for $H \parallel$ and $\perp c$. This reveals an overarching envelope of antiferromagnetic-like ordering, where the isotropic behavior is consistent with expectations for $L = 0$ magnetism. A greater variety of behavior is seen in the evolution of T_{N2}, which continuously

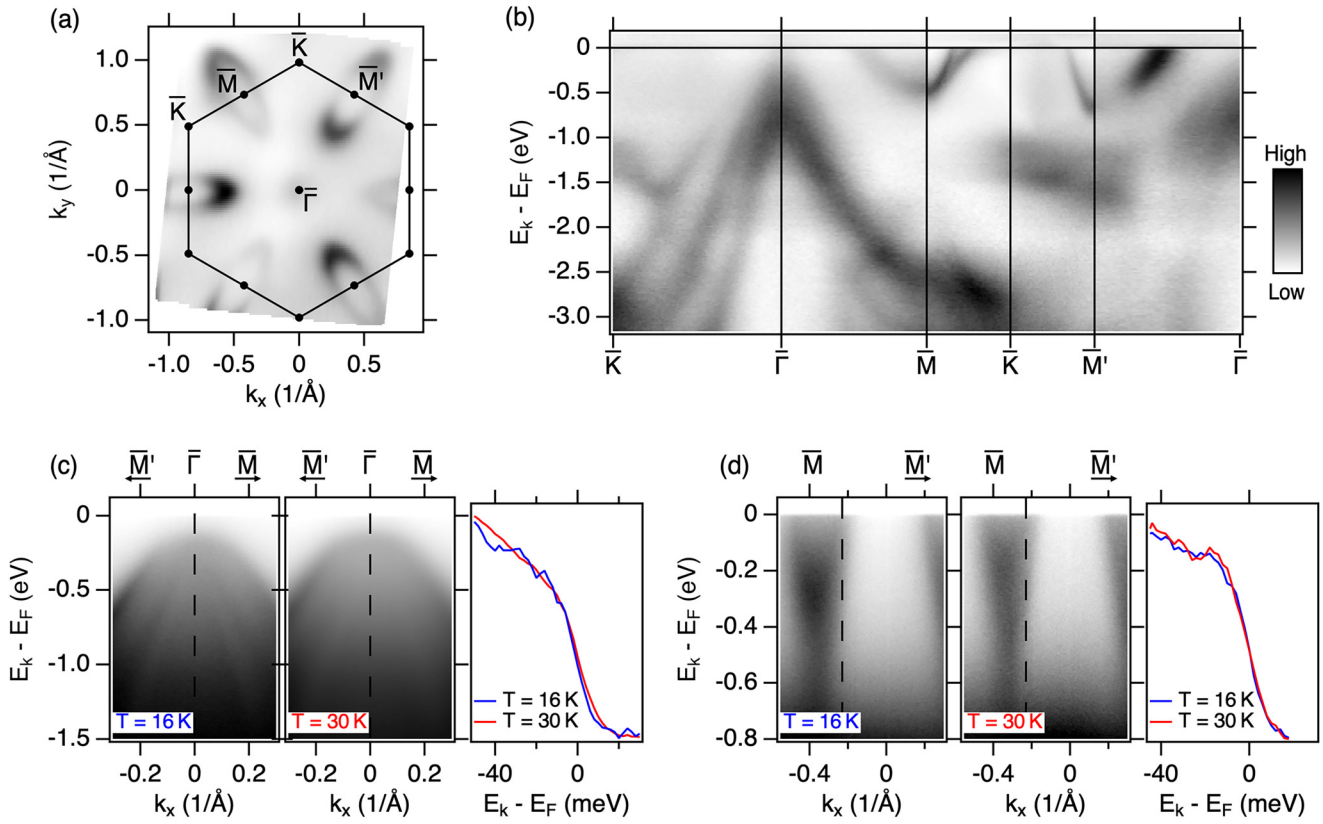

FIG. 6. Electronic structure of $GdAl_2Ge_2$ from ARPES Measurements. (a) Fermi surface at 16 K measured with a photon energy of hν = 45 eV. The data have been integrated around the Fermi level in an energy window between –35 meV and 5 meV. (b) Corresponding band structure along the $\bar{K}$-$\bar{\Gamma}$-$\bar{M}$-$\bar{K}$-$\bar{M}'$-$\bar{\Gamma}$ path. (c), (d) High-resolution ARPES measurements at 16 K and 30 K showing the band structure around the $\bar{\Gamma}$ and $\bar{M}$ points, respectively. The black dashed lines indicate the positions of the energy distribution curves (EDCs) shown in the final panels. Data in (c) and (d) were acquired with 20 eV photons and an experimental energy resolution better than 10 meV.

decreases for $H \parallel c$, but first increases before merging with T_{N1} for $H \perp c$. Increasing magnetic fields reveal several additional phase boundaries at lower temperatures. The first of these separates region II' from II, where II' tracks a hysteretic feature labeled H_1 in the magnetoresistance measurements. This reveals that the low-field ordered ground state includes magnetic domains and, thus, is not a simple antiferromagnetic arrangement of the spins. This is followed by the loss of hysteresis and evidence for a second phase boundary at H_2 that terminates between 2.5–3 T at low temperatures, above which a broad region labeled III is observed. From the magnetic susceptibility measurements, we find that this region is characterized by increased spin polarization, albeit without the full polarization that is seen upon crossing the phase boundary at T_{N1} into the paramagnetic state.

Broadly speaking, this behavior resembles what is seen in many other lanthanide metals, including CeSb [35], CeSbSe [36], $CeRu_2Al_2B$ [37], and $LnAuAl_4Ge_2$ (Ln = Nd, Sm, Tb) [25,26,38], whose behavior is understood to originate from finely balanced RKKY interactions. The plausibility of connecting the magnetic behavior to the geometry of the Fermi surface is also seen by contrasting the complex magnetic ordering of of $GdAl_2Ge_2$ with nonisoelectronic analogues, such as $EuAl_2Ge_2$. The latter exhibits simple A-type antiferromagnetism and has a Fermi surface of increased symmetry (i.e., sixfold) with respect to $GdAl_2Ge_2$ that is dominated by a central cylindrical feature and small petal-like features [39]. This difference at least partly results from europium being divalent while Gd is trivalent, thereby shifting the Fermi level to higher energies when Eu is replaced by Gd. As a consequence, the cylindrical feature formed by the hole-like states around $\bar{\Gamma}$, which is central to the Fermi surface of $EuAl_2Ge_2$, moves below the Fermi level in the Gd analog. The now-expanded "petal"-shaped features dominate the Fermi contours, thereby governing the interactions between the local magnetic moments and the conduction electrons. As discussed earlier, these petals exhibit the threefold symmetry of the $GdAl_2Ge_2$ Fermi surface, in contrast to the more isotropic Fermi surface of $EuAl_2Ge_2$. This change is directly linked to the emergence of competing magnetic interactions: the Fermi surface acts as a communication network mediating the RKKY interactions between local moments. Our results demonstrate that $GdAl_2Ge_2$, serving as a minimal model for RKKY-driven competition on a triangular lattice, promotes magnetic frustration and complex ordering. This is in stark contrast to the highly-symmetric case of $EuAl_2Ge_2$, which stabilizes a simple type-A antiferromagnetic ground state [39]. An intriguing comparison can also be made to Gd_2PdSi_3 and $GdRu_2Si_2$, where first-principles calculations and measurements show that the nesting features of the Fermi surfaces of these compounds dominate the RKKY interaction, leading to the emergence of helical single-q spin-spiral ground states and

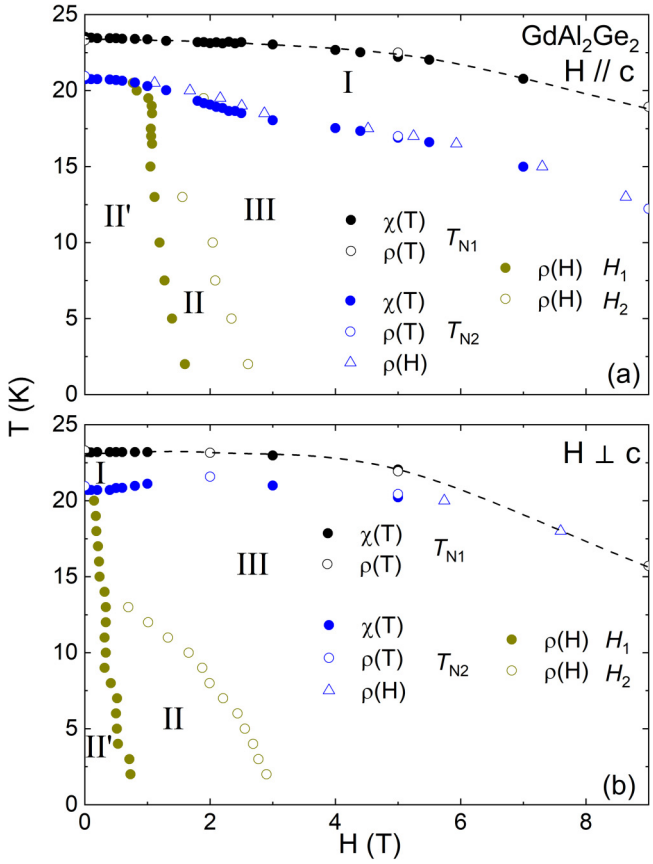

FIG. 7. Temperature T vs magnetic field H phase diagrams for $GdAl_2Ge_2$ constructed from magnetic susceptibility $\chi(T)$, heat capacity $C(T)$, and electrical resistivity $\rho(T, H)$ measurements. (a) H is applied along the c axis and (b) in the ab plane. The various regions labeled I, II, and III are described in the text, where region II' encompasses the region in which hysteresis is observed.

the stabilization of skyrmion lattices [7,15]. We thus propose that the magnetic ordering of $GdAl_2Ge_2$ is connected to the triangular symmetry of the Fermi surface, which provides opportunities for nontrivial magnetic ordering.

In the following, we further elaborate on our earlier observations concerning the interplay between magnetic ordering and Fermi surface symmetry. Looking beyond the phase diagram, what distinguishes $GdAl_2Ge_2$ from other RKKY-frustrated magnets is the disconnect between θ and T_N. To address this, we propose that the $L = 0$ characteristic of Gd produces conditions where the bare Fermi surface geometry dominates the formation of the ordered states. This is distinct from what is seen for other lanthanides where $L \neq 0$, which experience additional symmetry breaking because of spin-orbit coupling and the crystal electric field interaction. For $GdAl_2Ge_2$, this leads to competing interactions in the paramagnetic state and the resulting $\theta/T_{N1} << 1$. Support for this scenario is seen through comparisons to closely related compounds. For example, both $EuAl_2Ge_2$ [39] and $GdNiAl_4Ge_2$ [40] share the magnetic quantum numbers of $GdAl_2Ge_2$, but have $\theta/T_{N1} \approx 1$ and are characterized by highly symmetric Fermi surfaces with isotropic hole pockets around the zone center and rather tiny petal-like features around the M points. In contrast, $GdAuAl_4Ge_2$ has a Fermi surface that closely resembles that of $GdAl_2Ge_2$ [20] and shows $\theta/T_{N1} \ll 1$ [25]. From this, we conclude that the primary conditions that are necessary for the unusual θ/T_{N1} behavior of $GdAl_2Ge_2$ is that $L = 0$ and that the Fermi surface has symmetries that promote competing magnetic exchange interactions. In this sense, $GdAl_2Ge_2$ (and $GdAuAl_4Ge_2$) represent a generic environment for RKKY-driven magnetic competition, with the potential to produce mean-field breakdown in tandem with nontrivial magnetic ordering. Further measurements, such as Hall effect, neutron or x-ray scattering, and Lorentz microscopy, are still needed to explore this concept in more detail.

V. CONCLUSIONS

In summary, we have verified that $GdAl_2Ge_2$ crystallizes in the trigonal $CaAl_2Si_2$ structure ($P\bar{3}m1$), which we identify as being related to a broader homologous series that includes materials with the chemical formulas $LnTAl_4Ge_2$ (Ln = lanthanide) where the space group is rhombohedral ($R\bar{3}m$). Magnetization, heat capacity, and electrical transport measurements uncover complex magnetism in the T–H phase space, with a disconnect between the mean-field magnetic interaction and the magnetic ordering. This is discussed in the context of competing RKKY interactions mediated by conduction electrons in a Fermi surface of reduced symmetry. In this context, the $L = 0$ orbital quantum number for Gd ensures that symmetry breaking due to spin-orbit coupling and crystal electric field splitting are negligible, thereby ensuring that the Fermi surface itself is the most crucial factor determining paramagnetism and the appearance of ordered states. We thus introduce $GdAl_2Ge_2$ as a model system for further studies of complex magnetic ordering that may include nontrivial spin structures.

ACKNOWLEDGMENTS

R.E.B. acknowledges support from the University of California, Santa Cruz through startup funds. The authors acknowledge SOLEIL for the provision of synchrotron radiation under the Proposal No. 20240208 and the CASSIOPEE team for their support during our experiments. This work was supported by public grants from the French National Research Agency (ANR), projects SUPERNICKEL (No. ANR-21-CE30-0041-05), MICROVAN (No. ANR-24-CE30-3213-01) and FastNano (No. ANR-22-PEXD-0006), and by the CNRS International Research Project EXCELSIOR. J.Y.C., G.T.M., and M.G.A. were supported by the Welch Foundation (Grant No. AA-2056-20240404) and the National Science Foundation through NSF Grant No. DMR 2505304.

DATA AVAILABILITY

The data that support the findings of this article are not publicly available. The data are available from the authors upon reasonable request.

[1] C.-Z. Chang, C.-X. Liu, and A. H. MacDonald, *Colloquium*: Quantum anomalous Hall effect, Rev. Mod. Phys. **95**, 011002 (2023).

[2] A. Neubauer, C. Pfleiderer, B. Binz, A. Rosch, R. Ritz, P. G. Niklowitz, and P. Böni, Topological Hall effect in the a phase of MnSi, Phys. Rev. Lett. **102**, 186602 (2009).

[3] T. Kurumaji, T. Nakajima, M. Hirschberger, A. Kikkawa, Y. Yamasaki, H. Sagayama, H. Nakao, Y. Taguchi, T.-H. Arima, and Y. Tokura, Skyrmion lattice with a giant topological Hall effect in a frustrated triangular-lattice magnet, Science **365**, 914 (2019).

[4] M. Sato and Y. Ando, Topological superconductors: A review, Rep. Prog. Phys. **80**, 076501 (2017).

[5] S. Sasaki, M. Kriener, K. Segawa, K. Yada, Y. Tanaka, M. Sato, and Y. Ando, Topological superconductivity in $Cu_xBi_2Se_3$, Phys. Rev. Lett. **107**, 217001 (2011).

[6] B. R. Ortiz, S. M. L. Teicher, Y. Hu, J. L. Zuo, P. M. Sarte, E. C. Schueller, A. M. Milinda Abeykoon, M. J. Krogstad, S. Rosenkranz, R. Osborn, R. Seshadri, L. Balents, J. He, and S. D. Wilson, CsV_3Sb_5 : A $\mathbb{Z}_2$ topological kagome metal with a superconducting ground state, Phys. Rev. Lett. **125**, 247002 (2020).

[7] J. Bouaziz, E. Mendive-Tapia, S. Blügel, and J. B. Staunton, Fermi-surface origin of skyrmion lattices in centrosymmetric rare-earth intermetallics, Phys. Rev. Lett. **128**, 157206 (2022).

[8] N. Duy Khanh, T. Nakajima, X. Yu, S. Gao, K. Shibata, M. Hirschberger, Y. Yamasaki, H. Sagayama, H. Nakao, L. Peng, *et al.*, Nanometric square skyrmion lattice in a centrosymmetric tetragonal magnet, Nat. Nanotechnol. **15**, 444 (2020).

[9] S.-W. Cheong and F.-T. Huang, Altermagnetism classification, npj Quantum Mater. **10**, 38 (2025).

[10] J. Krempaský, L. Šmejkal, S. W. D' Souza, M. Hajlaoui, G. Springholz, K. Uhlířová, F. Alarab, P. C. Constantinou, V. Strocov, D. Usanov, *et al.*, Altermagnetic lifting of Kramers spin degeneracy, Nature (London) **626**, 517 (2024).

[11] L. Šmejkal, J. Sinova, and T. Jungwirth, Emerging research landscape of altermagnetism, Phys. Rev. X **12**, 040501 (2022).

[12] J.-Z. Ma, S. M. Nie, C. J. Yi, J. Jandke, T. Shang, M. Y. Yao, M. Naamneh, L. Q. Yan, Y. Sun, A. Chikina, *et al.*, Spin fluctuation induced Weyl semimetal state in the paramagnetic phase of $EuCd_2As_2$, Sci. Adv. **5**, eaaw4718 (2019).

[13] Y. Xu, L. Das, J. Z. Ma, C. J. Yi, S. M. Nie, Y. G. Shi, A. Tiwari, S. S. Tsirkin, T. Neupert, M. Medarde, M. Shi, J. Chang, and T. Shang, Unconventional transverse transport above and below the magnetic transition temperature in Weyl semimetal $EuCd_2As_2$, Phys. Rev. Lett. **126**, 076602 (2021).

[14] S. R. Saha, H. Sugawara, T. D. Matsuda, H. Sato, R. Mallik, and E. V. Sampathkumaran, Magnetic anisotropy, first-order-like metamagnetic transitions, and large negative magnetoresistance in single-crystal Gd_2PdSi_3, Phys. Rev. B **60**, 12162 (1999).

[15] Y. Dong, Y. Arai, K. Kuroda, M. Ochi, N. Tanaka, Y. Wan, M. D. Watson, T. K. Kim, C. Cacho, M. Hashimoto, D. Lu, Y. Aoki, T. D. Matsuda, and T. Kondo, Fermi surface nesting driving the RKKY interaction in the centrosymmetric skyrmion magnet Gd_2PdSi_3, Phys. Rev. Lett. **133**, 016401 (2024).

[16] W. Liu, Z. Zhang, J. Ji, Y. Liu, J. Li, X. Wang, H. Lei, G. Chen, and Q. Zhang, Rare-earth chalcogenides: A large family of triangular lattice spin liquid candidates, Chin. Phys. Lett. **35**, 117501 (2018).

[17] B. Schmidt, J. Sichelschmidt, K. M. Ranjith, T. Doert, and M. Baenitz, Yb delafossites: Unique exchange frustration of 4 f spin-1/2 moments on a perfect triangular lattice, Phys. Rev. B **103**, 214445 (2021).

[18] T. Xie, S. Gozel, J. Xing, N. Zhao, S. M. Avdoshenko, L. Wu, A. S. Sefat, A. L. Chernyshev, A. M. Läuchli, A. Podlesnyak, and S. E. Nikitin, Quantum spin dynamics due to strong Kitaev interactions in the triangular-lattice antiferromagnet $CsCeSe_2$, Phys. Rev. Lett. **133**, 096703 (2024).

[19] C. Kranenberg, D. Johrendt, and A. Mewis, The stability range of the $CaAl_2Si_2$-type structure in case of $LnAl_2Ge_2$ compounds, Solid State Sci. **4**, 261 (2002).

[20] C. Zhang, Y. Wang, F. Zhang, H. Rong, Y. Cai, L. Wang, X.-M. Ma, S. Guo, Z. Chen, Y. Wang, *et al.*, Multiple surface states, nontrivial band topology, and antiferromagnetism in $GdAuAl_4Ge_2$, Chin. Phys. B **32**, 077401 (2023).

[21] P. Rezende-Gonçalves, A. Antezak, T. Kato, K. Feng, F. Fortuna, P. Le Fèvre, M. Rosmus, N. Olszowska, T. Sobol, D. J. Singh, R. E. Baumbach, A. F. Santander-Syro, and E. Frantzeskakis, Metallic layered materials with magnetic frustration: An ARPES view of $SmAuAl_4Ge_2$ and $TbAuAl_4Ge_2$, Phys. Rev. B **111**, 205114 (2025).

[22] M. A. Ruderman and C. Kittel, Indirect exchange coupling of nuclear magnetic moments by conduction electrons, Phys. Rev. **96**, 99 (1954).

[23] T. Kasuya, A theory of metallic ferro- and antiferromagnetism on Zener's Model, Prog. Theor. Phys. **16**, 45 (1956).

[24] K. Yosida, Magnetic properties of Cu-Mn alloys, Phys. Rev. **106**, 893 (1957).

[25] K. Feng, I. A. Leahy, O. Oladehin, K. Wei, M. Lee, and R. Baumbach, Magnetic ordering in $GdAuAl_4Ge_2$ and $TbAuAl_4Ge_2$: Layered compounds with triangular lanthanide nets, J. Magn. Magn. Mater. **564**, 170006 (2022).

[26] K. Feng, C. Bush, O. Oladehin, M. Lee, and R. Baumbach, Complex antiferromagnetic order in the metallic triangular lattice compound $SmAuAl_4Ge_2$, Phys. Rev. B **109**, 014436 (2024).

[27] L. Krause, R. Herbst-Irmer, G. M. Sheldrick, and D. Stalke, Comparison of silver and molybdenum microfocus x-ray sources for single-crystal structure determination, J. Appl. Crystallogr. **48**, 3 (2015).

[28] G. M. Sheldrick, SHELXT–Integrated space-group and crystal-structure determination, Acta Crystallogr., Sect. A: Found. Adv. **71**, 3 (2015).

[29] G. M. Sheldrick, Crystal structure refinement with SHELXL, Acta Crystallogr., Sect. C: Struct. Chem. **71**, 3 (2015).

[30] See Supplemental Material at http://link.aps.org/supplemental/10.1103/kjct-68sj for data tables listing Table 1 for crystallographic data, data collection, and refinement parameters of $GdAl_2Ge_2$, Table 2 for atomic coordinates and displacement parameters for GdAl, (2Ge2), Table 3 for select interatomic distances (Å) of $GdAl_2Ge_2$, which includes Ref. [39].

[31] E. Gladyshevskii, Crystal structure of $CaAl_2Si_2$ and its analogs, Ukr. Fiz. Zh (Russ. Ed.) [Ukr. Phys. J.] **12**, 447 (1967).

[32] F. Gao, J. Sheng, W. Ren, Q. Zhang, X. Luo, J. Qi, M. Cong, B. Li, L. Wu, and Z. Zhang, Incommensurate spin density wave and magnetocaloric effect in the metallic triangular lattice $HoAl_2Ge_2$, Phys. Rev. B **106**, 134426 (2022).

[33] J. C. Lashley, M. F. Hundley, A. Migliori, J. L. Sarrao, P. G. Pagliuso, T. W. Darling, M. Jaime, J. C. Cooley, W. L.

Hults, L. Morales, *et al.*, Critical examination of heat capacity measurements made on a Quantum Design physical property measurement system, Cryogenics **43**, 369 (2003).

[34] S. Moser, An experimentalist's guide to the matrix element in angle resolved photoemission, J. Electron Spectrosc. Relat. Phenom. **214**, 29 (2017).

[35] J. Rossat-Mignod, P. Burlet, J. Villain, H. Bartholin, W. Tcheng-Si, D. Florence, and O. Vogt, Phase diagram and magnetic structures of CeSb, Phys. Rev. B **16**, 440 (1977).

[36] K.-W. Chen, Y. Lai, Y.-C. Chiu, S. Steven, T. Besara, D. Graf, T. Siegrist, T. E. Albrecht-Schmitt, L. Balicas, and R. E. Baumbach, Possible devil's staircase in the Kondo lattice CeSbSe, Phys. Rev. B **96**, 014421 (2017).

[37] R. E. Baumbach, H. Chudo, H. Yasuoka, F. Ronning, E. D. Bauer, and J. D. Thompson, $CeRu_2Al_2B$: A local-moment $4f$ magnet with a complex *T-H* phase diagram, Phys. Rev. B **85**, 094422 (2012).

[38] M. Cong, H. Ge, L. Zhang, W. Ren, N. Zhao, T. Li, S. Wang, J. Zhu, J. Mei, Q. Zhang, J. Sheng, F. Gao, B. Li, Z. Zhang, and L. Wu, Magnetic phase diagram and multiple field-induced states in the intermetallic triangular-lattice antiferromagnet $NdAuAl_4Ge_2$ with Ising-like spins, Phys. Rev. Mater. **7**, 024423 (2023).

[39] S. Pakhira, A. K. Kundu, F. Islam, M. A. Tanatar, T. Roy, T. Heitmann, T. Yilmaz, E. Vescovo, M. Tsujikawa, M. Shirai, R. Prozorov, D. Vaknin, and D. C. Johnston, Anisotropic magnetism and electronic structure of trigonal $EuAl_2Ge_2$ single crystals, Phys. Rev. B **107**, 134439 (2023).

[40] E. Frantzeskakis, A. Santander-Syro, and R. E. Baumbach (unpublished).